Article

Laboratory Measurements of Surface Wave Propagation through Ice Floes in Salt Water

Mark Orzech [1,*], Jie Yu [1], David Wang [1], Blake Landry [1], Carlo Zuniga-Zamalloa [1], Edward Braithwaite [1], Kathryn Trubac [2] and Callum Gray [3]

1   Ocean Sciences Division, U.S. Naval Research Laboratory, Stennis Space Center, MS 39529, USA
2   Cold Regions Research & Engineering Laboratory, U.S. Army Corps of Engineers, Hanover, NH 03755, USA
3   LaVision Inc., Ypsilanti, MI 48197, USA
*   Correspondence: mark.orzech@nrlssc.navy.mil

Abstract: Surface waves traversing polar marginal ice zones (MIZs) generate a boundary layer immediately below the ice, similar in some respects to the wave boundary layer created at the seabed in shallow water. The wave–ice boundary layer has not yet been thoroughly measured, but it can significantly affect wave attenuation rates. In December 2021, we conducted a laboratory experiment designed to measure such a boundary layer and the associated attenuation, in which monochromatic waves propagated through broken surface ice in a salt water tank. A particle imaging velocimetry (PIV) instrument array was submerged in the tank and used to visualize the fluid motion under the moving ice. The surface was tracked at multiple locations with acoustic sensors and cameras mounted over the tank. A total of 64 trials were completed, each producing 3–6 s of highly resolved velocity time series and 30–40 s of surface elevation data. Preliminary analysis of the data has provided strong evidence of a boundary layer at the water–ice interface. The wave attenuation rates compare well with existing datasets. The vertical profiles of RMS velocities and wave-induced Reynolds stress have trends similar to the theoretical predictions, while the quantitative discrepancies in terms of numerical values are discussed. This is the first of two such experiments; the second is tentatively scheduled for early 2023.

Keywords: wave experiment; surface ice; PIV; boundary layer; wave attenuation; marginal ice zone

1. Introduction

The interaction of ocean surface waves with ice floes in polar regions is a complex process about which much remains unknown. As the Earth's temperature continues to rise and the Arctic region becomes more navigable, it is increasingly important to understand and accurately predict both the ice effects on waves (e.g., wave attenuation and scattering) and the wave effects on ice (e.g., formation and growth of new ice, fracturing and retreat of ice sheets). In a feedback loop, ice retreat causes the wind–wave fetch to increase in the open ocean, which allows waves to grow more powerful and further damage the ice, accelerating the retreat rates [1–3]. In the spring and summer months, a growing proportion of the remaining Arctic ice cover turns into a field of fractured separate ice floes—what has typically been called the "marginal" ice zone (MIZ)—but increasingly spreads throughout the warmer Arctic region [4–6].

Over the past decade, a number of large-scale field efforts have examined the interactions of ocean waves and sea ice, e.g., [7–9]. The Arctic Sea State Departmental Research Initiative (DRI), sponsored by the Office of Naval Research (ONR), compiled a wealth of data on interacting air, ice, ocean, and wave processes and provided an excellent testing ground for state-of-the-art wave–ice models [8]. In the Antarctic, Kohout et al., [9] found an exponential attenuation of waves passing into MIZs, with rates proportional to the ice concentration.

A variety of laboratory experiments have also been conducted to measure the attenuation of waves in different types of ice under controlled conditions, e.g., [10–14]. Zhao and Shen [15] described results from a 2013 laboratory study of monochromatic waves in frazil, pancake, and fragmented ice covers, comparing the data with both viscous and viscoelastic dissipation models. Employing an optimization procedure with an inverse method to estimate effective ice viscosity and shear modulus from laboratory attenuation data, they demonstrated that different types of ice cover consistently corresponded to specific model parameters, suggesting that a direct relationship could ultimately be established between ice morphology and the associated representative viscosity and elasticity. Rogers et al., [16] noted that DRI field data for wave attenuation rates did not appear to align with the rates measured in small-scale laboratory experiments and hypothesized that there may be different physical mechanisms causing wave dissipation by sea ice for different frequency ranges. Yu et al., [17,18] found that ice thickness plays an important role in determining the wave attenuation rates, demonstrating that laboratory and field attenuation rates from various experiments collapse towards a general trend when they are normalized by ice thickness.

A variety of approaches have been attempted to model the propagation of waves through MIZs, many of which represent the broken surface ice cover as either a viscous or a viscoelastic layer [11,19–23]. The layer-based representations are generally tuned using measurements from selected laboratory and/or field datasets and have limited predictive capacity when applied to conditions different from those in the calibration. In continuum-based models, the dispersion relation is generally a highly transcendental function of many variables (i.e., the zero of the determinant of the coefficient matrix of a linear system). The complex wavenumber, which measures wave attenuation, is a function of frequency, but it is also dependent on other ice properties, including ice density, viscosity, elasticity, and thickness. Nevertheless, wave attenuation rates in most field experiments have still generally been presented as a function of just the wave frequency.

Zhao and Shen [24] examined the wave–ice interaction using a three-layer model, consisting of a viscoelastic ice layer on top, a viscous water boundary layer below it, and an inviscid ocean basin beneath the two. The approach was highly parameterized, requiring an inverse method to determine its parameters, and could not be used predictively. Nevertheless, it did demonstrate the separate and variable wave-damping effects of both the ice and the ice–water boundary layer. The authors called for more direct measurements of the properties of the boundary layer, including the eddy viscosity and the boundary layer thickness, in order to better understand these variations. Chen et al., (2019) [25] and Xu and Guyenne (2022) [26] developed a continuum porous viscoelastic model for wave attenuation by surface ice that included a dissipative frictional mechanism based on the relative motion of the fluid and the solid components of the ice cover. The mechanism, which reasonably reproduced wave "rollover" effects measured in the Arctic, might also be used as a surrogate for modeling the damping effects of a boundary layer underneath the ice.

When waves propagate through broken surface ice, a wave boundary layer develops at the ice–water interface and is likely turbulent due to eddies produced by the ice pieces interacting with the wave [5,7]. In a recent small-scale laboratory study, Rabault et al., [27] reported on eddy structures that they detected with PIV measurements, attributing their origin to the generation and diffusion of strong vortices by packs of drifting and colliding grease ice. This phenomenon is analogous to the boundary layer created by waves over viscous or viscoelastic mud. For the latter case, it has been shown that the boundary-layer-induced mass drift in mud can lead to resonances that amplify the mud motion and increase wave damping by some orders of magnitude, e.g., [28,29]. For the case of sea ice, it seems reasonable to anticipate that wave attenuation is also significantly affected by the wave-induced mass transport in the sub-ice boundary layer.

A preliminary study by Stopa et al., [2] related wave dissipation to the laminar and turbulent wave orbital velocities in the sub-ice wave boundary layer, achieving some success in hindcasting wave attenuation from the Sea State DRI data. However, the

nonlinear effects of the ice were not addressed in that paper, and a number of important model parameters, such as ice roughness and boundary layer velocities, were not carefully measured or validated. The wave-induced flow field and the associated fluid boundary layer under the ice play an important role in these interactions, but thus far they have almost exclusively been measured with only point-source instruments such as the acoustic Doppler velocimeter (ADV).

To more carefully investigate the wave–ice boundary layer and the associated flow field, we recently conducted a laboratory experiment in which monochromatic waves of varying amplitudes and frequencies were generated and allowed to propagate into broken surface ice. The experiment was designed to obtain evidence of such a boundary layer with detailed measurements of wave velocities under the ice and also to track the effects of the surface ice on wavelengths and amplitudes by monitoring the water surface elevation at multiple locations for waves of different periods and energy levels. It will be followed by a second experiment in which ice thickness and other properties will be configured to more closely match field scales (currently scheduled for February 2023).

This paper provides an overview of the first experiment and its initial results. Experimental configuration and methods are presented in Section 2 and results are summarized in Section 3. This is followed by additional discussion in Section 4 and overall conclusions in Section 5.

2. Materials and Methods

The tests were conducted in a salt water wave tank that was enclosed in a temperature-controlled facility at the US Army Corps of Engineers Cold Regions Research and Engineering Laboratory (CRREL) in Hanover, NH, USA. A primary goal of the experiment was to capture highly resolved records of the fluid velocity fields and the boundary layer that are produced as waves travel through broken ice floes mixed with frazil. To accomplish this, a particle imaging velocimetry (PIV) system was submerged beneath the surface ice, with its laser aimed upward.

To our knowledge, this is only the second such experiment to measure the three-dimensional fluid velocity fields generated under surface ice by wave motion. Rabault et al., [27] used a white LED lighting array together with 50-micron spherical seeding particles to record the velocity fields generated by waves propagating through grease ice in a small (3.5 m × 0.3 m × 0.25 m) wave tank located in a refrigerated facility in Norway. In a somewhat different configuration, Bushuk et al., [30] used a downward-facing PIV system similar to ours to investigate the small-scale formation of ice scallops along an inclined bed in a recirculating flume maintained at 0 °C. The PIV system employed in this study has also previously been utilized in a downward-facing configuration to measure sediment transport on a sandy seabed [31].

The three-week experiment was conducted within CRREL's Frost Effects Research Facility, a 2700 m^2 warehouse that was maintained at -7 °C or below for the entire period. Waves were generated by a flap-type wave maker in the Ice Wave Tank, an approximately 14 m × 2.5 m basin that was filled with salt water (salinity ≈ 33.4 ppt) to ~2 m depth (Figure 1). An ice layer was allowed to form on the water surface each night. Scraping tools were then used to detach the ice from the lateral walls in the morning before commencing wave tests. When the freezing occurred over a single night, it produced ice around 2 cm thick. When the freezing occurred over two nights (i.e., from Saturday afternoon to Monday morning), it resulted in ice of thickness ~5 cm.

The PIV system (Figure 2) was deployed on an aluminum base plate that was fixed to the tank bottom via a mounting platform and lead weights, with the plate center approximately 50 cm above the bottom of the tank, 150 cm below the water surface, and 270 cm from the wave paddle. The system consisted of an upward-pointing solid-state class IV laser paired with a rotating mirror that fanned the beam to create a triangular sheet of light, which expanded to approximately 70 cm width at a distance 1.5 m above the instrument. Two mounted cameras were used to acquire PIV image pairs from the

fanned laser region, tracking the motion of seeding particles in the plane of the beam to determine fluid velocities in three dimensions. The laser and cameras were all enclosed in sealed "bottles" and the camera bottles were filled with nitrogen gas to minimize the fogging of lenses. Acoustic sensors were mounted above the tank at different distances from the wave paddle and used to measure oscillations of the free or ice-covered surface and the associated wave attenuation in each test. Sensors s4 and s5 (Figure 1) were added later in the experiment. Sensor s1 was positioned over open water, while all other sensors were over the surface ice. Two GoPro video cameras were also mounted along the lateral sides of the tank and compiled a video record of the surface for each test.
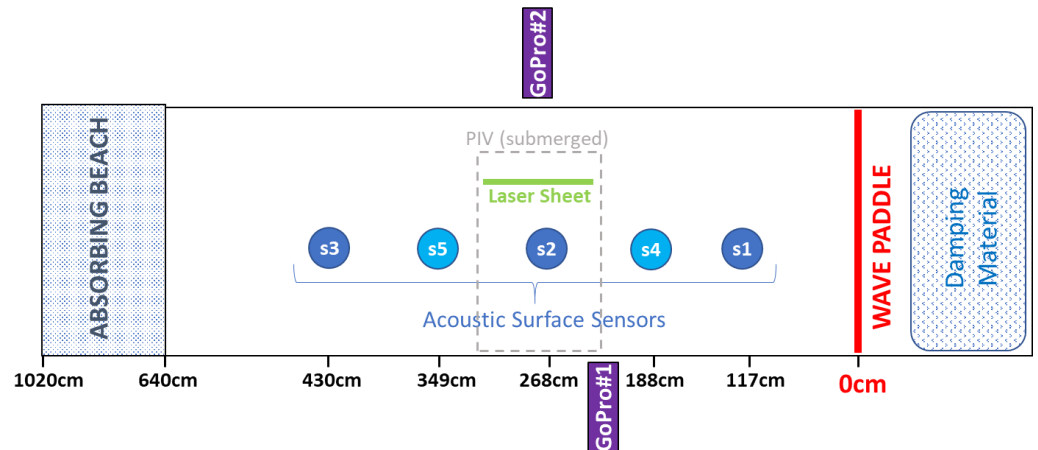

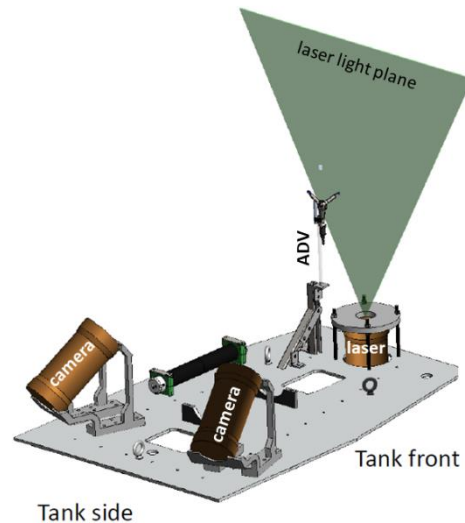**Figure 1.** Experimental layout, plan view.

Figure 2. Diagram of PIV configuration (central processing module not shown).

The wavemaker was configured to generate eight different monochromatic wave types, including two different periods and four different heights (Table 1). With a tank depth of 2 m, all the waves were essentially in deep water. The wavemaker and the acoustic sensors were activated at the same time, while the PIV system was activated approximately 3 s later and allowed to record data for approximately 3–6 s (2–6 wave periods). The recording was shut off before any waves reflected from the far end of the tank could return to the measurement area. For each individual test, the wavemaker was run for 40 s and then stopped to allow the water surface to become quiescent.

Table 1. Wavemaker settings for the 8 trials of each test series (period, height).

| 1	2	3	4	5	6	7	8
1 s, 2 cm	1 s, 4 cm	1 s, 6 cm	1 s, 8 cm	1.5 s, 2 cm	1.5 s, 4 cm	1.5 s, 6 cm	1.5 s, 8 cm

3. Results

In total, we recorded 64 trials, obtaining eight complete sets of data for each of the eight wave types (Table 2). In these datasets, the ice thickness varied from 0–5 cm, with ice-free open water for the first test series and scattered floes and frazil (e.g., Figure 3) for the remainder of the tests. Relative to the waves, the floes were generally thicker than those normally seen at field scales and thus more similar to a finite surface layer than to thin elastic plates. The ice consistently appeared unconsolidated and did not show evidence of columnar structure (Figure 4).

Table 2. Experiment details.

Test Series	Trial Numbers	Ice Thickness (cm)	Ice Config	No. of Elevation Sensors	Water Depth (cm)	Seeding Size (μ)
A	1–8	0.0	Ice-free	3	200	10
B	9–16	2.2	Floes/Frazil	3	200	100
C	17–24	3.8	Floes/Frazil	3	200	100
D	25–33 **	2.8	Floes/Frazil	3	200	100
E	34–42 **	3.8	Floes/Frazil	3	212	60
F	43–51 **	5.2	Floes/Frazil	3	212	60
G	52–59	3.0	Floes/Frazil	5	212	60
H	60–67	3.0	Floes/Frazil	5	212	100

** Trial numbers 28, 38, and 50 were discarded.
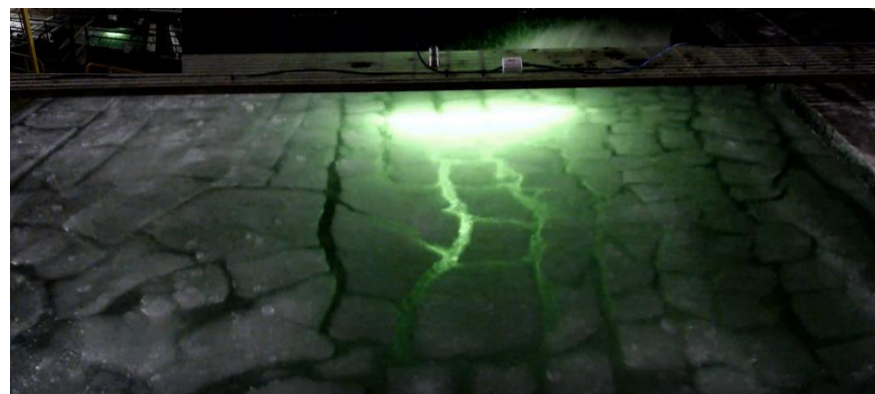
Figure 3. View of wave tank surface in the middle of a test.

Figure 4. Sample of 5 cm-thick ice.

After the wavemaker was turned on, there was a ramping-up period of several seconds before the configured amplitude was reached. Because of this, the PIV measurements were

initiated approximately 3 s after the wavemaker, allowing us to capture the prescribed wave motion while also avoiding reflected waves. Once the configured amplitude was reached, the "steady state" wave heights measured by the altimeters then tended to vary somewhat (5–10 percent) around the target height. Some of this variation was due to the effects of the shifting surface ice on the altimeter readings. Measured wave periods were consistently within 0.1 s of the nominal wavemaker settings.

3.1. Wave Attenuation in Ice

Wave attenuation is estimated through an analysis of surface elevation time series measured by the acoustic sensors s2 and s3. The complex wavenumber k may be written as $k = k_r + ik_i$, where k_r is the real wavenumber relating to the wave speed and k_i describes the attenuation rate. The e-folding distance of wave amplitude decay is $1/k_i$. For this analysis, the wave amplitude attenuation between the sensors is calculated as

$$k_i = \frac{1}{\Delta X_{23}} \ln\left(\frac{H_2}{H_3}\right), \tag{1}$$

where $\Delta X_{23} = 1.62$ m is the distance between the two sensors and H_j is the mean wave height at location j. The mean wave heights are determined by averaging over 4–6 waves, and averaging is stopped before the waves reflected from the back of the tank reach either sensor (similar to [12,14,32]). Wave attenuation was detected in 47 of the 56 trials, with surface-ice present (the signal in some trials was disrupted by noise). For the positive cases, we find a mean attenuation coefficient of 1.6×10^{-1} m^{-1}, with individual attenuation coefficients ranging between 1.4×10^{-3} and 6.6×10^{-1} m^{-1}. This result is roughly in agreement with those obtained in laboratory experiments by Wang and Shen [11], who worked with grease and pancake ice, and Zhao and Shen [15], whose experiments included broken ice floes along with grease ice and pancakes. When the overall results are grouped by wave frequency ω, with $\omega_1 = 2\pi/(1\text{s})$ and $\omega_{1.5} = 2\pi/(1.5\text{s})$ (Figure 5a), they show a greater mean attenuation for the 1 s waves ($k_{i,1} = 2.5 \times 10^{-1}$ m^{-1}) than for the 1.5 s waves ($k_{i,1.5} = 5.8 \times 10^{-2}$ m^{-1}), as expected.
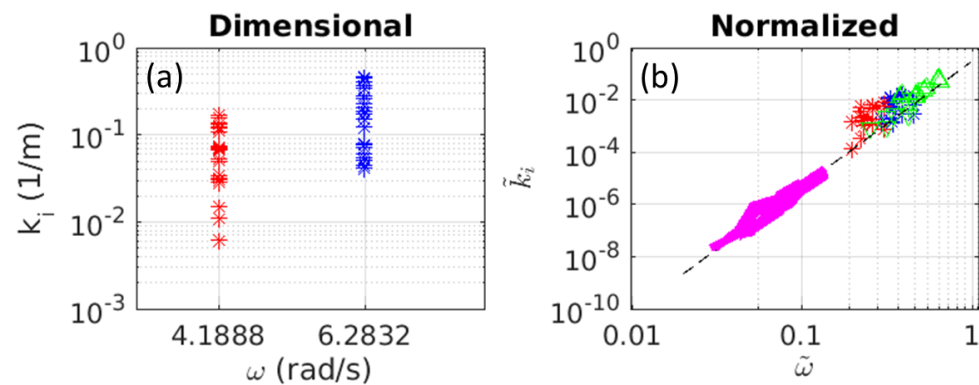
Figure 5. Estimated attenuation coefficients for 47 of 56 cases, grouped by wave period (red: T = 1.5 s, blue: T = 1 s). Panel (**a**): dimensional data on semilogy axes. Panel (**b**): the same datasets normalized using (2) and (3), on log–log axes together with field data from PIPERS experiment [33] (magenta lines) and laboratory data from [11] (upward green triangles) and [24] (downward green triangles). Black dashed best-fit line was computed using (4).

Following the procedure of [17], we recast these attenuation rates in a dimensionless format by normalizing with the ice thickness (Figure 5b). The normalized attenuation coefficient and wave frequency, respectively, are given by

$$\widetilde{k}_i = k_i \cdot h, \tag{2}$$

$$\widetilde{\omega} = \omega \cdot \sqrt{h/g}, \tag{3}$$

where h is ice thickness (m) and g is the gravitational constant. Plotted together with our normalized data are results from similar laboratory experiments by [11,15], as well as field data from the PIPERS experiment [33]. The black dashed line in this panel corresponds to the empirical best-fit relationship

$$\widetilde{k}_i = 0.2805\widetilde{\omega}^{4.8}, \tag{4}$$

which was derived by [34] for the combined field and laboratory data (not including our results). Although our attenuation estimates include some uncertainty in the surface elevations ($\pm 5\%$) owing to the measurement noise described above, they are nevertheless very similar to the other laboratory results. Thus, the collapsing of our dataset onto the monomial fit (4) in the dimensionless plan ($\widetilde{k}_i$, $\widetilde{\omega}$) is an indication that the experimental conditions are also relevant to those of field waves in sea ice (at least not dissimilar). For the follow-up experiment, we are considering the deployment of an acoustic current profiler (ADCP) to validate PIV velocity fields and to obtain an alternate water level dataset.

3.2. Ice Effects on Real Wavenumber k_r

In this section, we compare experimental results for the wave number in ice, k_r, to predictions based on the viscous layer theory [17,34]. Using the altimeter data at sensors 2 and 3, we estimated k_r following the procedure outlined in [32]. For each trial, we compared the time series from the two sensors and determined the time required (Δt) for a selected wave crest to travel the distance from sensor 2 to sensor 3 ($\Delta x = 1.62$ m). The wave phase speed was then determined as $c = \Delta x / \Delta t$. Making use of the relationship

$$c = 2\pi f / k_r, \tag{5}$$

in which $f = 1/T$ is the wave frequency (1 Hz or 0.67 Hz, depending on the specific trial); we then solved for the wave number. Here we present sample results from three out of the eight test series that were least disrupted by instrument noise or timing issues.

The selected series, B, C, and F in Table 2, feature a range of ice thickness values: 2.2, 3.8, and 5.2 cm, respectively. For each test series, we found that the mean wave number consistently increased in the ice with increasing frequency. In Figures 6 and 7, these results are compared in both a dimensional and a non-dimensional form to theoretical curves based on the viscous layer theory [17–19,34].

The dimensional results in Figure 6 include three theoretical curves (magenta lines), corresponding to the ice thicknesses measured in cases B, C, and F, respectively. Also shown is the solution from the linear theory for waves in open water (i.e., without the ice cover). Experimental results are displayed as colored circles, each with estimated error ranges (vertical bars).

The non-dimensional form of the real wavenumber is now computed for these data as $\widetilde{k}_r = k_r h$, and the non-dimensional frequency $\widetilde{\omega}$ is calculated using (3). For the non-dimensionalized results shown in Figure 7, the theoretical curves of Figure 6 collapse together and are practically indistinguishable from the solution for open water. Once normalized by the associated ice thickness, the measured data are within the error limits of the single theoretical curve, although the result for the thickest ice (series F, $h = 5.2$ cm) deviates somewhat more than the others.

3.3. PIV Data: Velocity Fields

At depths of more than a few cm below the surface ice, the 2D velocity fields captured by the PIV system appear to be generally in accordance with the expected behavior, showing clear evidence of wave motion (Figure 8). However, the PIV measurements in this region are partially disrupted by the ice layer (e.g., broken white line in Figure 8), which occasionally causes anomalously large and/or misdirected velocity estimates for areas in the vicinity of the surface ice. The processing of these data to mark and remove such erroneous points has been complex and time-consuming. We are currently developing an algorithm to automate

the marking of the lower ice boundary in each PIV image. In the following sections, we present the processed PIV results from a single representative case: trial 18 in test series C, for which the wave period was 1 s and the wave height was 4 cm.

Examples of quality-controlled PIV velocity fields at several time steps are provided in Figure 9. Velocities in the top 2.5 cm of each panel have been zeroed to minimize contamination by the surface ice. The propagation of the one-second waves (from right to left in the images) is evident from the evolving velocity fields. Although the depth range of each image is only about 10 cm, this is deep enough to show the tapering of the velocity magnitude with depth (i.e., $V_{mag} \sim e^{k_r z}$) that would be expected for the 1-s waves of this case. [1] Evidence of a boundary layer is also apparent in Figure 9, where the larger vertical gradient of velocity magnitudes near the ice interface contrasts markedly with the smooth gradual tapering predicted by the theory. Additional characteristics of this boundary layer will be investigated with the calculation of the RMS velocity profiles in Section 3.4.2.
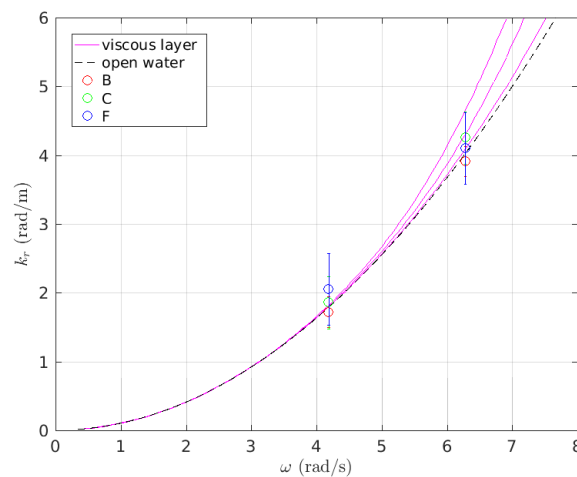

Figure 6. Wave number in ice k_r versus wave frequency ω. Average results from three test series are shown as circles with error bars. Also included are theoretical results based on the viscous layer theory [34], computed for the ice thickness in each of the three test series (magenta lines), and linear theory for open water (dashed black line). Viscous layer curves used an effective viscosity of $0.02 \text{ m}^2/\text{s}$.
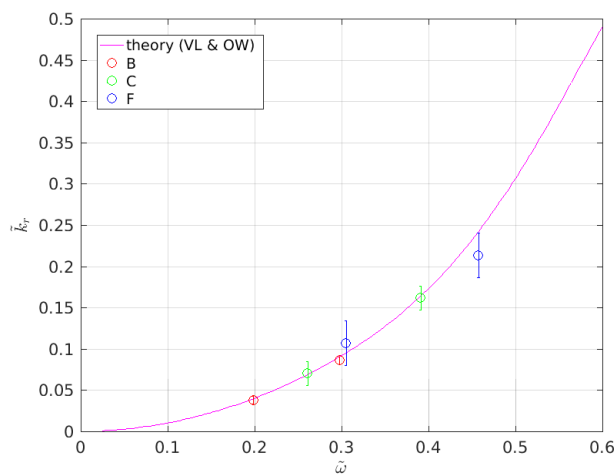

Figure 7. Non-dimensional wave number in ice $\widetilde{k}_r$ versus wave frequency $\widetilde{\omega}$, normalized using (2) and (3). Average results from three test series are shown as circles with error bars. Also included are non-dimensionalized theoretical results for the viscous layer theory (using the same configuration as in Figure 6) and the open water theory. Both theoretical results follow the same curve. The viscous layer curve again used an effective viscosity of $0.02 \text{ m}^2/\text{s}$.
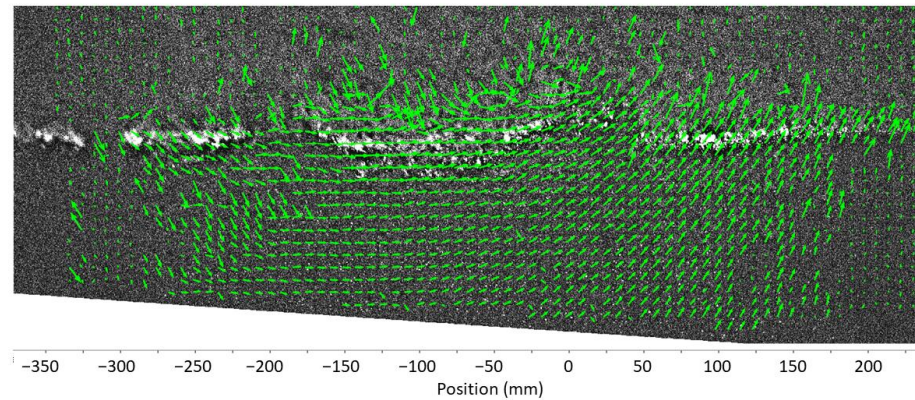
Figure 8. Sample PIV velocity field (raw image, no quality control), measuring approximately 60 cm width and 20 cm height. Orbital velocity fields (green arrows) are generated by waves propagating from right to left. The underside of the surface ice is visible as a fuzzy white line near the vertical center of the image. Data are from trial 18.
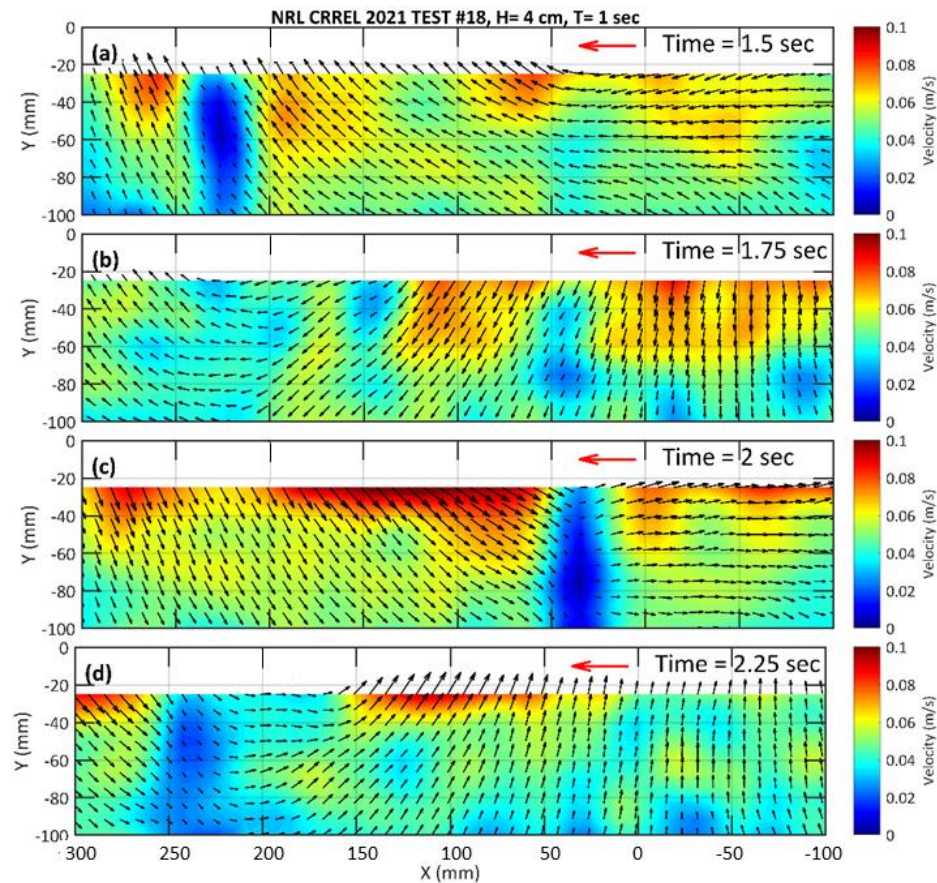
Figure 9. Instantaneous under-ice velocity fields from PIV measurements at time steps of (**a**) 1.5 s, (**b**) 1.75 s, (**c**) 2 s, and (**d**) 2.25 s. Colors represent velocity magnitudes. The coordinate X is the distance along the tank. The wavemaker is located beyond the right edge of the image, at X = −268 cm. (Note that the X-axis direction in these processed results has been flipped from that shown for the raw data in Figure 8.) The coordinate Y is the vertical distance to the mean water line of the tank. Black arrows indicate the flow direction and the velocity magnitude is indicated by the arrow length and color shadings. The red arrow indicates the wave propagation direction. Data are again from trial 18.

3.4. PIV Data: Analysis

3.4.1. Selection of Optimal Sampling Frequency

During initial processing, the water velocity components were obtained from PIV data by determining the displacements of seeding particles between images at different time steps. Several time intervals were used for these estimates. The highest image sampling frequency at which the velocity data were computed was approximately 348 Hz (i.e., a time step of ~0.003 s), using consecutive images. Additional velocity datasets were also generated for frequencies of 174, 87, 43.5, 21.75, and 10.875 Hz, by comparing images at greater increments. An automated quality control procedure was used to remove anomalous results (i.e., extremely large or misdirected velocities).

The selection of an optimal sampling frequency involves a trade-off between noise and data resolution. In this analysis, we have found that data sampled at higher frequencies are noisier and their individual data points appear less reliable, but the general trend of the data is well represented. In contrast, data sampled at lower frequencies are smoother but sometimes exhibit gaps, where the dominant signal is not captured at all.

A comparison of the along-tank velocity time series obtained using two different PIV sample rates at two different water depths is shown in Figure 10. The results were recorded at X = 2 cm in the PIV images of trial 18, for which the ice thickness was 3.8 cm, the wave period was 1 s, and the wave amplitude was approximately 2 cm. Although clearly noisier, the higher frequency data (f_s = 348 Hz) clearly do a better job of capturing the general trend and amplitude of the primary wave velocity at the shallower depth ($z = -4$ cm). The performance of the two sampling frequencies is comparable at the greater depth ($z = -11$ cm), although there is a much smoother result for the lower frequency data (f_s = 43.5 Hz).
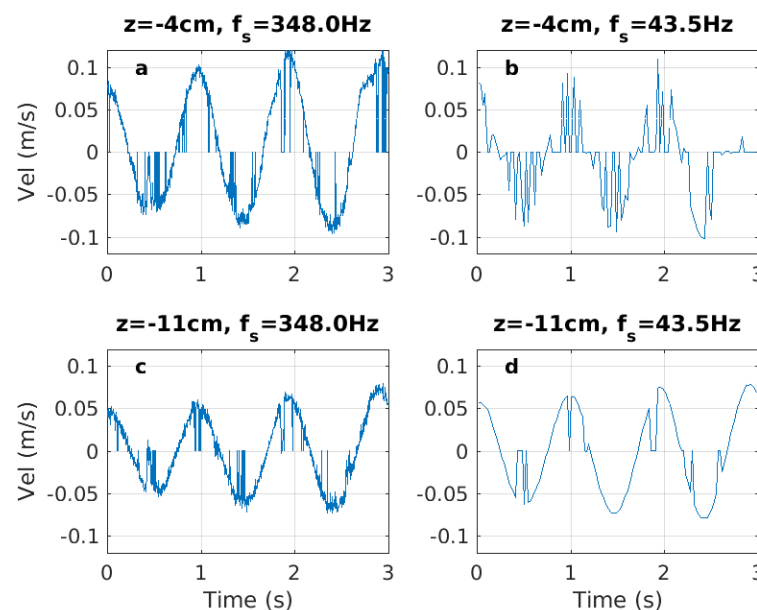
Figure 10. Along-tank velocity time series from trial 18, determined from PIV data using two different sampling rates at two different depths near the center of each image (X ≈ 2 cm). Left panels (**a**,**c**) use a sample rate of 348 Hz. Right panels (**b**,**d**) use a sample rate of 43.5 Hz. Top panels (**a**,**b**) show velocities at 4 cm below mean water level (MWL). Bottom panels (**c**,**d**) show velocities at 11 cm below MWL. (NB: for times when data are rejected, the time series are set to zero).

The PIV data analysis conducted in this paper is primarily focused on obtaining vertical profiles of RMS velocity and Reynolds stress (Section 3.4.2). The measured total velocity in Figure 10 clearly includes contributions at two time scales, i.e., a slower primary

oscillation (~1 Hz) and a very fast scale noise. Thus, we can decompose the total velocity into a wave component u_w and a turbulent component u_t, i.e.,

$$u = u_w + u_t. \tag{6}$$

The RMS velocity may then be calculated as

$$u_{RMS} = \sqrt{\langle u^2 \rangle} = \sqrt{\langle u_w^2 \rangle + 2\langle u_w u_t \rangle + \langle u_t^2 \rangle}, \tag{7}$$

where the angle brackets denote the time average. The components u_w and u_t are not strongly correlated because of the separation in their time scales, so $<u_w u_t> \approx 0$. If the turbulent component is small relative to the wave component, we can approximate $u_{RMS} \approx \sqrt{\langle u_w^2 \rangle}$, from which the velocity amplitude can be determined as $u_a = \sqrt{2} \cdot u_{RMS}$.

For the purpose of inferring velocity amplitudes, and in view of the scale separation between u_w and u_t, we apply a low-pass filter to each raw time series, effectively removing the turbulence and additional noise and leaving primarily the wave signal. To compare the performance of the two sampling rates examined above (i.e., 348 Hz and 43.5 Hz), a filter accepting only frequency components below 5 Hz is applied to each time series from Figure 10. The resulting "wave" components are shown in Figure 11. For the time series with a high sampling rate, the filtered data retain the wave signal in the 1-s scale quite well at both shallow and deep depths (see Figures 10a,c and 11a,c). For the time series sampled at a lower rate, however, the filtered data do not represent the 1-s wave oscillation well at $z = -4$ cm near the ice layer, missing most wave crests and troughs (see Figures 10b and 11b) and leading to an underestimated velocity amplitude. At the deeper depth where the turbulent fluctuation is weak, the filtered time series for the low sampling rate is similar to that for the high sampling rate, clearly showing the wave signal. We thus have chosen to use the high frequency PIV data in the analysis that follows.
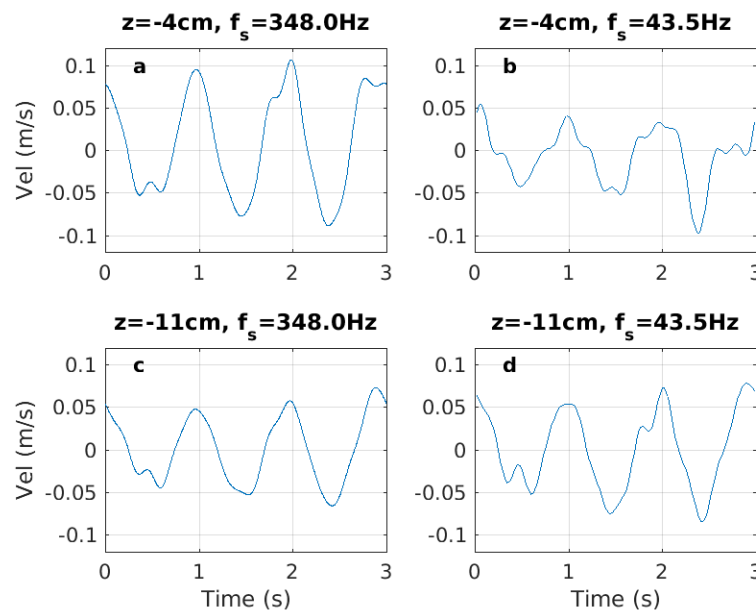
Figure 11. Low-pass filtered PIV-velocity time series for same two depths and two PIV-sampling frequencies as in Figure 10 above. In each case, data with frequencies over 5 Hz are now removed. Left panels (**a,c**) use a sample rate of 348 Hz. Right panels (**b,d**) use a sample rate of 43.5 Hz. Top panels (**a,b**) show velocities at 4 cm below mean water level (MWL). Bottom panels (**c,d**) show velocities at 11 cm below MWL.

3.4.2. Vertical Profiles of RMS Velocities and Reynolds Stress

The trial 18 PIV velocity data at X = 2 cm are now further processed to determine the profiles of RMS horizontal and vertical velocity (i.e., u_{RMS} and v_{RMS}) as well as Reynolds stress. The 348 Hz velocity time series for each component are obtained for a vertical transect extending from the lowest depth with data ($z \approx -14$ cm) to the estimated still-water surface ($z \approx 0$ cm). As described in the preceding section, the time series at each depth level are low-pass filtered (keeping frequencies below 5 Hz) to remove turbulent fluctuations and noise. Thus, the calculated RMS velocities correspond to

$$u_{RMS} = \sqrt{\langle u_w^2 \rangle}, \; v_{RMS} = \sqrt{\langle v_w^2 \rangle}, \tag{8}$$

where u_w and v_w now represent the primary wave component of the along-tank and the vertical velocity, respectively. The Reynolds stresses in the along-tank plane are calculated separately for the wave and turbulent velocity components as

$$\tau_{uv,w} = \langle u_w \cdot v_w \rangle, \; \tau_{uv,t} = \langle u_t \cdot v_t \rangle \tag{9}$$

where the turbulent components u_t and v_t are determined using a high-pass filter that retains only velocity data above 5 Hz.

Results are presented in Figures 12 and 13 below. The upper 2.5 cm of each figure are shaded gray to represent the region where the ice was determined to consistently corrupt the PIV data (as seen earlier in Figure 9). Immediately below this is an additional region in which the vertically oscillating ice interface only intermittently interfered with the measurements. Combining the velocity and the altimeter time series with the ice thickness data, we estimated that the lowest elevation reached by the interface in this trial was roughly $z = -4.5$ cm (i.e., ~2 cm wave amplitude plus ~2.5 cm ice below surface). This level is indicated by the black dotted line in each of the two figures. Between 2.5 and 4.5 cm below the surface, there was additional noise in the velocity signal (an example of which was provided for 4 cm depth in Figure 10a,b above). As we have demonstrated that this noise can largely be removed by applying a low-pass filter to the high-frequency PIV time series, we feel that the RMS velocity and the Reynolds stress estimates computed here are accurate in this region and below (while, in contrast, we cannot fully trust the results above $z = -2.5$ cm). We would expect that evidence of a boundary layer will primarily be found in the vicinity of this intermittent ice region.

Figure 12 shows profiles of the along-tank and vertical components of RMS velocity (i.e., u_{RMS} and v_{RMS}; solid lines), compared with the profile for the potential flow that would be expected under a linear wave of the same amplitude and period but in open water (i.e., $u, v \sim e^{k_r z}$; dashed line). In deeper depths (e.g., $z < -10$ cm), both RMS velocity profiles are fairly close to the open-water results, as expected. However, near the ice layer (e.g., $z = -3$ to -8 cm), the u_{RMS} velocity profile noticeably deviates from the open-water result, with a slope much greater than that expected from the theory. This suggests a boundary layer flow in the region. In contrast, the profile of the RMS vertical velocity v_{RMS} remains much closer to the open-water curve, as would be expected. Further upward (e.g., $z > -2.5$ cm), the PIV measurements are more consistently interrupted by the floating ice floes/packs, and the RMS velocity estimates are no longer considered accurate.

The Reynolds stress profiles for the wave and turbulent components of the measured velocity time series were calculated following (9), using the same velocity time series at the same location as the RMS velocities (Figure 13). The Reynolds stress τ_w induced by the wave fluctuations for this case is generally much greater than that produced by the turbulent fluctuations, consistent with the observation in Figure 10a,c that the time series are dominated by the nearly sinusoidal wave oscillation of 1 s. Again, we are most confident in the profile data below $z = -2.5$ cm. These results will be discussed further in Section 4.
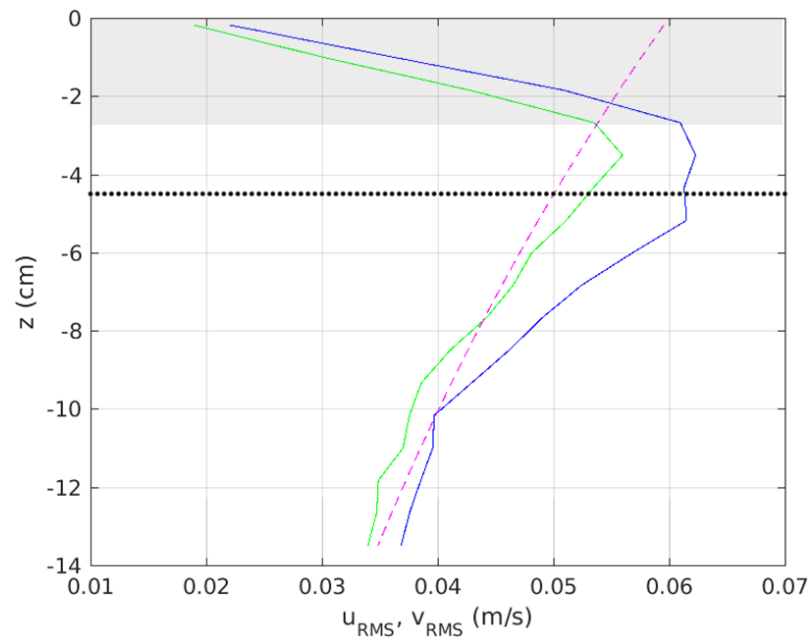
Figure 12. RMS velocity profiles computed from PIV velocity measurements under ice in trial 18, including u_{RMS} (blue), v_{RMS} (green), and theoretical profile for waves of this type in ice-free open water (magenta dashed). Black dotted line represents approximate lowest depth reached by ice–water interface; gray shaded region is depth range in which PIV data were corrupted by ice layer (see text).
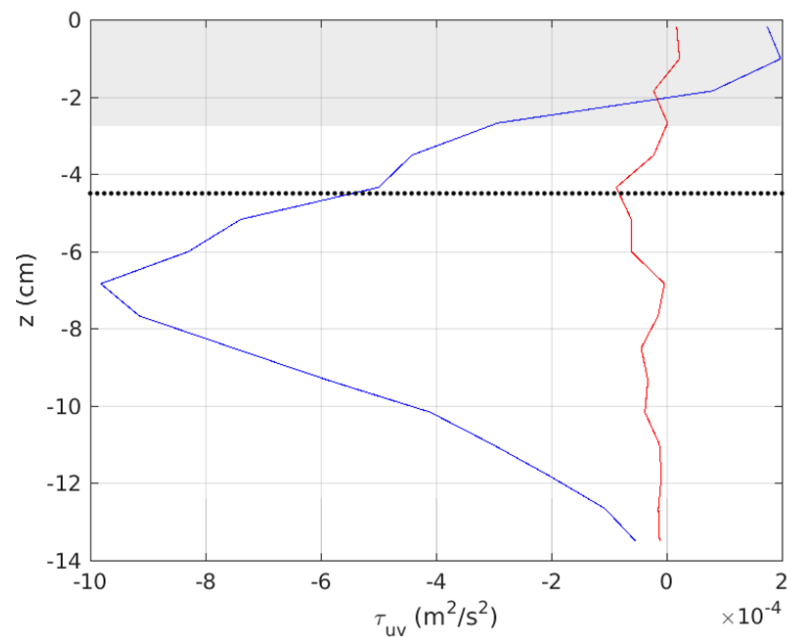
Figure 13. Near-surface Reynolds stress profile for PIV velocity time series at $X = 2$ cm in trial 18, separated into wave (blue, $f < 5$ Hz) and turbulent (red, $f > 5$ Hz) contributions. Note that the direction of positive u velocity in this figure is toward the right, in contrast to Figure 9. Black dotted line represents approximate lowest depth reached by ice–water interface; gray shaded region is depth range in which PIV data were corrupted by ice layer (see text).

4. Discussion

The estimates of wave attenuation in ice obtained in Section 3.1 were for wave frequencies of 0.67 and 1.0 Hz and ice thicknesses between 2.2–5.2 cm, conditions that are generally larger in scale than those used in earlier laboratory experiments of this nature. As

was illustrated in Figure 5, the normalized wave-to-ice scales of these data were generally somewhat closer to those of field data (i.e., had smaller $\widetilde{\omega}$ and $\widetilde{k}_i$) in comparison to the results of [11,15]. This indicates that the combined condition of waves and ice in the CRREL experiments is more similar to some field conditions. As Yu et al., [18] pointed out, the fact that datasets with different scales of wave and ice collapse towards the general trend suggests the existence of similarity between field and laboratory observations. That is, Equation (4) alternatively expresses the condition of similarity from the dimensional analysis perspective. This may be seen as follows. For frequency ω, the open-water dispersion relation is $\omega^2 = gk_{ow}$ for deep-water waves, where k_{ow} is the open-water wavenumber. Equation (4) can be rewritten using k_{ow} as

$$k_i/k_{ow} = 0.2805(k_{ow}h)^{2.4}. \tag{10}$$

For a laboratory model to be similar to a specific set of field conditions, it means that

$$\frac{(k_i/k_{ow})_{fld}}{(k_i/k_{ow})_{lab}} = \frac{(k_{ow}h)^{2.4}_{fld}}{(k_{ow}h)^{2.4}_{lab}}, \tag{11}$$

assuming that the gravitational acceleration g is same in the laboratory and the field. Thus, a 1-s laboratory wave propagating in 3.8 cm ice may be said to experience a similar relative attenuation rate (k_i/k_{ow}) to that of a 5-s field wave in 37 cm of ice. In the upcoming second experiment, we will attempt to reduce our ice thickness values to ~1 cm in order to more closely approach similarity to the measured field conditions in the Arctic Sea State experiment (for which wave periods were often significantly greater than 5 s and ice thickness mostly closer to 10 cm). Specific Sea State data will be selected in advance of the follow-up experiment, and laboratory wave and ice parameters will be configured to match scaled-down field values.

The effect of ice on the wavelength (i.e., changing the real wavenumber k_r) was determined for selected test series in Section 3.2. As estimated from the altimeter data, the wavenumber values in ice were well predicted by theoretical curves based on the viscous layer theory and all were within the estimated measurement error. The effect of ice thickness on these results was illustrated by plotting them first in dimensional form (Figure 6) and then in a normalized format (Figure 7). The test series that deviated most from the non-dimensionalized theoretical viscous-layer curve (i.e., series F) also featured the thickest ice floes ($h = 5.2$ cm). The more extreme relative conditions of this test series (i.e., $h = 65\%$ to 260% of wave amplitude and 1% to 3% of wavelength) may have contributed to increased errors in the altimeter-based estimates of wave phase velocity.

Processed PIV velocity fields and vertical profiles of RMS velocities and Reynolds stresses were presented in Sections 3.3 and 3.4. As evident from the "raw" PIV data in Figure 8, the velocity data were sometimes corrupted in the vicinity of the surface ice. It was necessary to determine the vertical extent of this layer ($z = -2.5$ cm) and to exclude velocities above it in order to obtain a relatively "clean" dataset (Figure 9). By carefully marking the surface layer in every PIV image, it may eventually be possible to determine water velocities immediately adjacent to the moving ice interface with a surface-following analysis, which would produce the most accurate measurement of the boundary layer. This processing method is very time-consuming and beyond the scope of the present paper; such results will be provided in a future article.

As illustrated in Section 3.4.1, the optimal method for processing PIV velocity data is dictated by the specific goals of the analysis. Velocity vectors are determined by comparing locations of seeding particles in different PIV images at a selected increment or time step, and this increment may vary from 1 (i.e., comparing consecutive images) to a much larger value dictated by the time scales being measured. The largest increment utilized for these data was 32, corresponding to a PIV sampling frequency of just over 10 Hz. As we were working with surface waves of frequency 0.67–1 Hz, this sampling rate would still allow us

to obtain at least 10 data points per wave period, enough to resolve each individual wave oscillation reasonably well. Lower increments, of course, obtain a better resolution of the primary wave signal but are correspondingly noisier, as was discussed above.

Above, we examined two time-averaged statistics of the wave motion, RMS velocity and Reynolds stress, seeking evidence of a wave boundary layer immediately below the ice–water interface. For this specific goal, we required accurate estimates of the amplitude of the dominant wave oscillation. With low-pass filtering, the highest frequency (increment 1) PIV time series was shown to better capture the primary wave signal near the ice than did a lower frequency (increment 8) time series (Figures 10 and 11).

A simple validation of the high frequency processing method selected in Section 3.4.1 can be performed by examining the RMS velocities of Section 3.4.2 at the same two elevations. From Figure 11a, we can visually estimate the amplitude of the velocity at depth $z = -4$ cm to be approximately 0.09 m/s over the analyzed 3-s time period. From Figure 11c, we similarly find an amplitude of approximately 0.055 m/s at $z = -11$ cm. As noted in Section 3.4.1, the velocity amplitude is related to the RMS velocity as $u_a = \sqrt{2} \cdot u_{RMS}$. From Figure 12, we find the values of u_{RMS} at $z = -4$ cm and -11 cm to be 0.062 m/s and 0.04 m/s, respectively, hence obtaining $u_a = 0.089$ m/s and 0.056 m/s, respectively. As expected, these compare very well with the values estimated by visual examination of the time series. The surface wave amplitude A may be computed from these values with the linear theory via the deep-water relationship

$$u_a = A\omega e^{k_r z}, \tag{12}$$

as the water depth $H \approx 2$ m is greater than the wavelength $L \approx 1.56$ m for this case. Solving for A with each of the two velocity amplitudes and depths, we estimate a value of 1.7 cm using velocity data at $z = -4$ cm and 2.0 cm using data at $z = -11$ cm. The waves for this case (trial 18) had a nominal amplitude of 2 cm, which was confirmed ($\pm$ 5–10%) by the altimeter-measured surface elevation data.

The large gradient that was identified in the RMS along-tank velocity u_{RMS} provides evidence of the existence of a wave-generated boundary layer just beneath the ice (Figure 12). This measured profile exhibits features similar to the theoretical solutions for linear waves in two fluid layers with a viscous layer overlaying the lower viscosity water [34], examples of which are provided in Figure 14a. Specifically, in both the measured and the theoretical profiles, the velocity magnitude (i) increases with depth in the region immediately above the lower ice–water boundary (dotted line), (ii) begins to rapidly decrease with increasing depth from a point just underneath this boundary, at a rate steeper than that given by the theory of a potential linear wave motion, and (iii) tends to follow the linear open water theory solution at deeper locations farther away from the interface.

In contrast to both theoretical profiles, the measured result is more broadly spread out in the vertical direction, having a milder gradient and a thicker boundary layer. This is likely a consequence of enhanced eddy activities and subsequent turbulent mixing in the vicinity of the ice–water interface, which tends to erase sharp gradients (as diffusion does) and acts to increase the effective (or apparent) water viscosity (ν_w) near the interface. Supporting this hypothesis, the gradient of the experimental profile below the ice in Figure 12 is closer to that of the blue curve in Figure 14a, which was computed using a value of ν_w that was one-tenth the viscosity of the ice (i.e., $\nu_w = \nu_i/10$). In contrast, the green curve with the steeper gradient was computed with a much smaller water eddy viscosity (i.e., $\nu_w = \nu_i/100$). While the turbulent component of the wave motion was relatively small in comparison to the main wave signal (Figure 13), it was not negligible in the region just below the ice, where the associated Reynolds stress reached ten percent of that induced by the waves.

The wave-induced Reynolds stress profile computed for trial 18 is also qualitatively similar to theoretical profiles for different ice-to-water viscosity ratios, as illustrated by a comparison of Figure 13 with Figure 14b. In both the laboratory measurements and in the theoretical results, the wave-induced Reynolds stresses are near zero at greater depths and become increasingly negative as we move up towards the interface. As with RMS velocities, we again find that the measured wave-induced Reynolds stress profile in Figure 13 is

closer in shape to the blue curve in Figure 14b, which was also computed for a higher water viscosity (i.e., $\nu_w = \nu_i/10$). This provides additional evidence that turbulence in the laboratory tank increased the water viscosity in the region immediately below the ice.
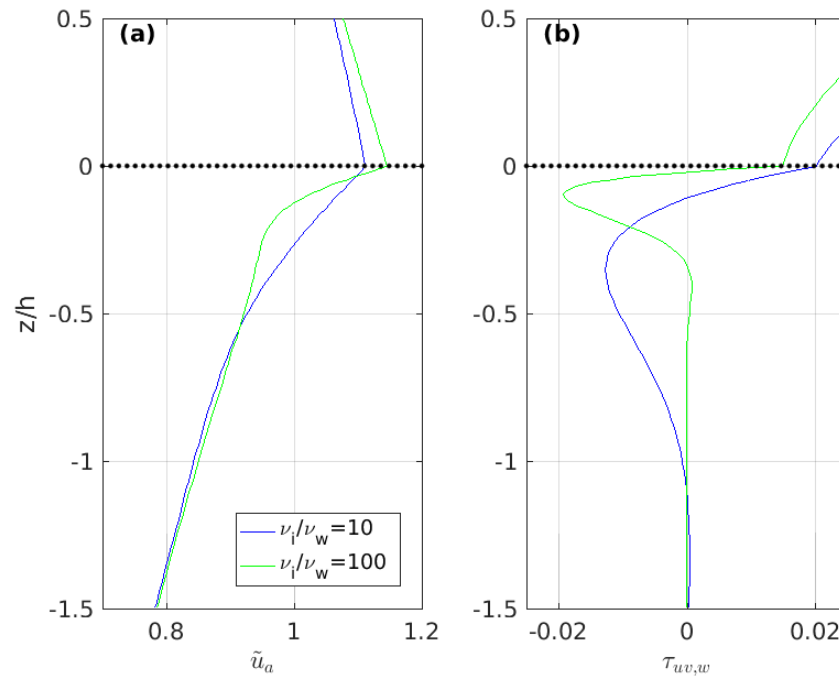
Figure 14. Theoretical solutions from the linear theory of waves in two layers of fluid with a viscous ice layer overlaying less viscous water [34]: (**a**) vertical profiles of velocity amplitude $\hat{u}_a$, (**b**) the corresponding wave-induced Reynolds stress $\tau_{uv,w}$, where u and v are the linear fluid velocities of the wave motion. Note that, in contrast to Figures 12 and 13, the minimum depth reached by the ice—water interface is designated $z = 0$ on these panels (dotted line). The velocities are normalized by $|v(z = 0)|$ (i.e., the vertical velocity magnitude at $z = 0$). The normalization does not change the shape of the profiles. As in [34], relative ice viscosity and thickness values are prescribed by Reynolds number $R_e = h\sqrt{gh}/\nu_i = 5$, with two values of ice/water viscosity ratio, ν_i/ν_w. The dimensionless frequency $\widetilde{\omega} = 0.4$.

5. Conclusions

We have conducted a set of tests in which monochromatic surface waves propagated through surface ice in a laboratory tank filled with salt water. We used an innovative PIV system submerged in the tank to record velocity fields under the ice with high spatial and temporal resolution, and we employed acoustic sensors above the ice to track the surface elevation at multiple locations. Estimated wave attenuation is very similar to that seen in other comparable laboratory experiments and is close to model predictions. PIV-measured velocity fields capture the oscillations due to the propagating waves and the variation of velocity magnitudes with depth. Initial results provide evidence of a wave boundary layer at the ice–water interface. Vertical profiles of RMS velocity and Reynolds stress exhibit variations with depth and vertical extent that are similar to those obtained from the theory.

This experiment has demonstrated that it is possible to compile highly resolved datasets of velocity fields generated by waves passing under surface ice with a submerged PIV system, and it has produced reasonable estimates of wave attenuation rates and fluid velocity profiles. Data from additional trials continue to be processed and we expect to provide more comprehensive results in a future paper. Much remains to be investigated using these techniques, which will be modified and improved in the upcoming second experiment.

Notes

[1] From Figure 6, it is clear that $k_r \approx 4.0 \text{ m}^{-1}$ for the 1-s waves of this case. Thus, we expect wave velocity to have attenuated by a factor of approximately $e^{k_r z} = e^{4.0 \cdot (-0.1)} \approx 0.67$ at 10-cm depth, great enough to be clearly visible.

References

1. Thomson, J.; Rogers, W.E. Swell and sea in the emerging Arctic Ocean. *Geophys. Res. Lett.* **2014**, *41*, 3136–3140. [CrossRef]
2. Stopa, J.E.; Ardhuin, F.; Girard-Ardhuin, F. Wave climate in the Arctic 1992–2014: Seasonality and trends. *Cryosphere* **2016**, *10*, 1605–1629. [CrossRef]
3. Comiso, J.C.; Meier, W.N.; Gersten, R. Variability and trends in the Arctic Sea ice cover: Results from different techniques. *J. Geophys. Res. Ocean.* **2017**, *122*, 6883–6900. [CrossRef]
4. Strong, C.; Rigor, I.G. Arctic marginal ice zone trending wider in summer and narrower in winter. *Geophys. Res. Lett.* **2013**, *40*, 4864–4868. [CrossRef]
5. Aksenov, Y.; Popova, E.E.; Yool, A.; Nurser, A.G.; Williams, T.D.; Bertino, L.; Bergh, J. On the future navigability of Arctic sea routes: High-resolution projections of the Arctic Ocean and sea ice. *Mar. Policy* **2017**, *75*, 300–317. [CrossRef]
6. Squire, V.A. Ocean wave interactions with sea ice: A reappraisal. *Ann. Rev. Fluid Mech.* **2020**, *52*, 37–60. [CrossRef]
7. Lee, C.M.; Cole, S.; Doble, M.; Freitag, L.; Hwang, P.; Jayne, S.; Jeffries, M.; Krishfield, R.; Maksym, T.; Maslowski, W. *Marginal Ice Zone (MIZ) Program: Science and Experiment Plan*; APL-UW TR 1201; Technical Report; Applied Physics Laboratory-UW: Seattle, WA, USA, 2012; p. 48.
8. Thomson, J.; Ackley, S.; Girard-Ardhuin, F.; Ardhuin, F.; Babanin, A.; Boutin, G.; Brozena, J.; Cheng, S.; Collins, C.; Doble, M.; et al. Overview of the Arctic Sea State and Boundary Layer Physics Program. *J. Geophys. Res. Oceans* **2018**, *123*, 8674–8687. [CrossRef]
9. Kohout, A.L.; Smith, M.; Roach, L.A.; Williams, G.; Montiel, F.; Williams, M.J.M. Observations of exponential wave attenuation in Antarctic sea ice during the PIPERS campaign. *Ann. Glaciol.* **2020**, *61*, 196–209. [CrossRef]
10. Martin, S.; Kauffman, P. A field and laboratory study of wave damping by grease ice. *J. Glaciol.* **1981**, *27*, 283–313. [CrossRef]
11. Wang, R.; Shen, H.H. Experimental study on surface wave propagating through a grease–pancake ice mixture. *Cold Reg. Sci. Technol.* **2010**, *61*, 90–96. [CrossRef]
12. Sree, D.K.; Law, A.W.-K.; Shen, H.H. An experimental study on gravity waves through a floating viscoelastic cover. *Cold Reg. Sci. Technol.* **2018**, *155*, 289–299. [CrossRef]
13. Marchenko, A.; Haase, A.; Jensen, A.; Lishman, B.; Rabault, J.; Evers, K.-U.; Shortt, M.; Thiel, T. Laboratory investigations of the bending rheology of floating saline ice, and physical mechanisms of wave damping, in the HSVA ice tank. *arXiv* **2019**, arXiv:1901.05333.
14. Yiew, L.; Parra, S.; Wang, D.; Sree, D.; Babanin, A.; Law, W.K.A. Wave attenuation and dispersion due to floating ice covers. *Appl. Ocean Res.* **2019**, *87*, 256–263. [CrossRef]
15. Zhao, X.; Shen, H.H. Wave propagation in frazil/pancake, pancake, and fragmented ice covers. *Cold Reg. Sci. Technol.* **2015**, *113*, 71–80. [CrossRef]

16. Rogers, W.E.; Posey, G.P.; Li, L.; Allard, R.A. *Forecasting and Hindcasting Waves in and Near the Marginal Ice Zone: Wave Modeling and the ONR "Sea State" Field Experiment*; U.S. Naval Research Laboratory Report NRL/MR/7320-18-9786; US Naval Research Laboratory: Washington, DC, USA, 2018; p. 179. Available online: https://ww7320.nrlssc.navy.mil/pubs.php (accessed on 25 June 2022).

17. Yu, J.; Rogers, W.E.; Wang, D.W. A Scaling for Wave Dispersion Relationships in Ice-Covered Waters. *J. Geophys. Res. Oceans* **2019**, *124*, 8429–8438. [CrossRef]

18. Yu, J.; Rogers, W.E.; Wang, D.W. A new method for parameterization of wave dissipation by sea ice. *Cold Reg. Sci. Technol.* **2022**, *199*, 103582. [CrossRef]

19. Keller, J.B. Gravity waves on ice-covered water. *J. Geophys. Res.* **1998**, *103*, 7663–7669. [CrossRef]

20. De Carolis, G.; Desiderio, D. Dispersion and attenuation of gravity waves in ice: A two-layer viscous fluid model with experimental data validation. *Phys. Lett. A* **2002**, *305*, 399–412. [CrossRef]

21. Mosig, J.E.M.; Montiel, F.; Squire, V.A. Comparison of viscoelastic-type models for ocean wave attenuation in ice-covered seas. *J. Geophys. Res. Oceans* **2015**, *120*, 6072–6090. [CrossRef]

22. Meylan, M.H.; Bennetts, L.; Mosig, J.; Rogers, W.; Doble, M.J.; Peter, M.A. Dispersion Relations, Power Laws, and Energy Loss for Waves in the Marginal Ice Zone. *J. Geophys. Res. Oceans* **2018**, *123*, 3322–3335. [CrossRef]

23. Doble, M.J.; De Carolis, G.; Meylan, M.H.; Bidlot, J.; Wadhams, P. Relating wave attenuation to pancake ice thickness, using field measurements and model results. *Geophys. Res. Lett.* **2015**, *42*, 4473–4481. [CrossRef]

24. Zhao, X.; Shen, H.H. Three-layer viscoelastic model with eddy viscosity effect for flexural-gravity wave propagation through ice cover. *Ocean Model.* **2018**, *131*, 15–23. [CrossRef]

25. Chen, H.; Gilbert, R.P.; Guyenne, P. Dispersion and attenuation in a porous viscoelastic model for gravity waves on an ice-covered ocean. *Eur. J. Mech. B/Fluids* **2019**, *78*, 88–105. [CrossRef]

26. Xu, B.; Guyenne, P. Assessment of a porous viscoelastic model for wave attenuation in ice-covered seas. *Appl. Ocean Res.* **2022**, *122*, 103122. [CrossRef]

27. Rabault, J.; Sutherland, G.; Jensen, A.; Christensen, K.H.; Marchenko, A. Experiments on wave propagation in grease ice: Combined wave gauges and particle image velocimetry measurements. *J. Fluid Mech.* **2019**, *864*, 876–898. [CrossRef]

28. Ng, C.-O. Mass transport and set-ups due to partial standing surface waves in a two-layer viscous system. *J. Fluid Mech.* **2004**, *520*, 297–325. [CrossRef]

29. Ng, C.-O.; Zhang, X. Mass transport in water waves over a thin layer of soft viscoelastic mud. *J. Fluid Mech.* **2007**, *573*, 105–130. [CrossRef]

30. Bushuk, M.; Holland, D.M.; Stanton, T.P.; Stern, A.; Gray, C. Ice scallops: A laboratory investigation of the ice–water interface. *J. Fluid Mech.* **2019**, *873*, 942–976. [CrossRef]

31. Landry, B.L.; Mieras, R.; Key, C.; Braithwaite, E.F.; Gray, C.; Griffin, S.; Calantoni, J. Adapting laboratory instrumentation to observe sand ripple dynamics in the nearshore. In *AGU Fall Meeting Abstracts*; American Geophysical Union: Washington, DC, USA, 2018.

32. Parra, S.M.; Sree, D.K.; Wang, D.; Rogers, E.; Lee, J.H.; Collins, C.O.; Law, A.W.-K.; Babanin, A.V. Experimental study on surface wave modifications by different ice covers. *Cold Reg. Sci. Technol.* **2020**, *174*, 103042. [CrossRef]

33. Ackley, S.F.; Stammerjohn, S.; Maksym, T.; Smith, M.; Cassano, J.; Guest, P.; Tison, J.-L.; Delille, B.; Loose, B.; Sedwick, P.; et al. Sea-ice production and air/ice/ocean/biogeochemistry interactions in the Ross Sea during the PIPERS 2017 autumn field campaign. *Ann. Glaciol.* **2020**, *61*, 181–195. [CrossRef]

34. Yu, J. Wave boundary layer at the ice-water interface. *J. Mar. Sci. Eng.* **2022**, *10*, 1472. [CrossRef]